

# The Heavy Photon Search Test Detector

M. Battaglieri<sup>a</sup>, S. Boyarinov<sup>b</sup>, S. Bueltmann<sup>c</sup>, V. Burkert<sup>b</sup>, A. Celentano<sup>a</sup>, G. Charles<sup>f</sup>, W. Cooper<sup>d</sup>, C. Cuevas<sup>b</sup>, N. Dashyan<sup>e</sup>, R. DeVita<sup>a</sup>, C. Desnault<sup>f</sup>, A. Deur<sup>b</sup>, H. Egriyan<sup>b</sup>, L. Elouadrhiri<sup>b</sup>, R. Essig<sup>g</sup>, V. Fadeyev<sup>h</sup>, C. Field<sup>i</sup>, A. Freyberger<sup>b</sup>, Y. Gershtein<sup>j</sup>, N. Gevorgyan<sup>e</sup>, F.-X. Girod<sup>b</sup>, N. Graf<sup>i</sup>, M. Graham<sup>i</sup>, K. Griffioen<sup>k</sup>, A. Grillo<sup>h</sup>, M. Guidal<sup>f</sup>, G. Haller<sup>i</sup>, P. Hansson Adrian<sup>i,\*</sup>, R. Herbst<sup>i</sup>, M. Holtrop<sup>l</sup>, J. Jaros<sup>i</sup>, S. Kaneta<sup>b</sup>, M. Khandaker<sup>m</sup>, A. Kubarovsky<sup>n</sup>, V. Kubarovsky<sup>b</sup>, T. Maruyama<sup>i</sup>, J. McCormick<sup>i</sup>, K. Moffeit<sup>i</sup>, O. Moreno<sup>h</sup>, H. Neal<sup>i</sup>, T. Nelson<sup>i</sup>, S. Niccolai<sup>f</sup>, A. Odian<sup>i</sup>, M. Oriunno<sup>i</sup>, R. Paremuzyan<sup>e</sup>, R. Partridge<sup>i</sup>, S. K. Phillips<sup>l</sup>, E. Rauly<sup>f</sup>, B. Raydo<sup>b</sup>, J. Reichert<sup>j</sup>, E. Rindel<sup>f</sup>, P. Rosier<sup>f</sup>, C. Salgado<sup>m</sup>, P. Schuster<sup>o</sup>, Y. Sharabian<sup>b</sup>, D. Sokhan<sup>p</sup>, S. Stepanyan<sup>b</sup>, N. Toro<sup>o</sup>, S. Uemura<sup>i</sup>, M. Ungaro<sup>b</sup>, H. Voskanyan<sup>e</sup>, D. Walz<sup>i</sup>, L. B. Weinstein<sup>c</sup>, B. Wojtsekhowski<sup>b</sup>

<sup>a</sup>Istituto Nazionale di Fisica Nucleare, Sezione di Genova e Dipartimento di Fisica dell'Università, 16146 Genova, Italy

<sup>b</sup>Thomas Jefferson National Accelerator Facility, Newport News, Virginia 23606

<sup>c</sup>Old Dominion University, Norfolk, Virginia 23529

<sup>d</sup>Fermi National Accelerator Laboratory, Batavia, IL 60510-5011

<sup>e</sup>Yerevan Physics Institute, 375036 Yerevan, Armenia

<sup>f</sup>Institut de Physique Nucléaire d'Orsay, IN2P3, BP 1, 91406 Orsay, France

<sup>g</sup>Stony Brook University, Stony Brook, NY 11794-3800

<sup>h</sup>Santa Cruz Institute for Particle Physics, University of California, Santa Cruz, CA 95064

<sup>i</sup>SLAC National Accelerator Laboratory, Menlo Park, CA 94025

<sup>j</sup>Rutgers University, Department of Physics and Astronomy, Piscataway, NJ 08854

<sup>k</sup>The College of William and Mary, Department of Physics, Williamsburg, VA 23185

<sup>l</sup>University of New Hampshire, Department of Physics, Durham, NH 03824

<sup>m</sup>Norfolk State University, Norfolk, Virginia 23504

<sup>n</sup>Rensselaer Polytechnic Institute, Department of Physics, Troy, NY 12181

<sup>o</sup>Perimeter Institute, Ontario, Canada N2L 2Y5

<sup>p</sup>University of Glasgow, Glasgow, G12 8QQ, Scotland, UK

---

## Abstract

The Heavy Photon Search (HPS), an experiment to search for a hidden sector photon in fixed target electroproduction, is preparing for installation at the Thomas Jefferson National Accelerator Facility (JLab) in the Fall of 2014. As the first stage of this project, the HPS Test Run apparatus was constructed and operated in 2012 to demonstrate the experiment's technical feasibility and to confirm that the trigger rates and occupancies are as expected. This paper describes the HPS Test Run apparatus and readout electronics and its performance. In this setting, a heavy photon can be identified as a narrow peak in the  $e^+e^-$  invariant mass spectrum, above the trident background or as a narrow invariant mass peak with a decay vertex displaced from the production target, so charged particle tracking and vertexing are needed for its detection. In the HPS Test Run, charged particles are measured with a compact forward silicon microstrip tracker inside a dipole magnet. Electromagnetic showers are detected in a PbWO<sub>4</sub> crystal calorimeter situated behind the magnet, and are used to trigger the experiment and identify electrons and positrons. Both detectors are placed close to the beam line and split top-bottom. This arrangement provides sensitivity to low-mass heavy photons, allows clear passage of the unscattered beam, and avoids the spray of degraded electrons coming from the target. The discrimination between prompt and displaced  $e^+e^-$  pairs requires the first layer of silicon sensors be placed only 10 cm downstream of the target. The expected signal is small, and the trident background huge, so the experiment requires very large statistics. Accordingly, the HPS Test Run utilizes high-rate readout and data acquisition electronics and a fast trigger to exploit the essentially 100% duty cycle of the CEBAF accelerator at JLab.

**Keywords:** silicon, microstrip, tracking, vertexing, heavy photon, dark photon, electromagnetic calorimeter

---

1    **1. Introduction**

2    The heavy photon ( $A'$ ), aka a “hidden sector” or  
3    “dark” photon, is a massive particle which couples  
4    weakly to electric charge by mixing with the Standard  
5    Model photon [1, 2]. Consequently, it can be radiated  
6    by electrons and subsequently decay into  $e^+e^-$  pairs, al-  
7   beit at rates far below those of QED trident processes.  
8    Heavy photons have been suggested by numerous be-  
9   yond Standard Model theories [3], to explain the dis-  
10   crepancy between theory and experiment of the muon’s  
11    $g - 2$  [4], and as a possible explanation of recent as-  
12   trophysical anomalies, e.g. [5, 6, 7]. Heavy photons  
13   couple directly to hidden sector particles with “dark”  
14   or “hidden sector” charge; these particles could consti-  
15   tute all or some of the dark matter, e.g. [8, 9]. Current  
16   phenomenology highlights the  $20 - 1000 \text{ MeV}/c^2$  mass  
17   range, and suggests that the coupling to electric charge,  
18    $\epsilon e$ , has  $\epsilon$  in the range of  $10^{-3} - 10^{-5}$ . This range of pa-  
19   rameters makes  $A'$  searches viable in medium energy  
20   fixed target electroproduction [10], but requires large  
21   data sets and good mass resolution to identify a small  
22   mass peak above the copious QED background. At  
23   small couplings, the  $A'$  become long-lived, so detection  
24   of a displaced decay vertex can reject the prompt QED  
25   background and boost experimental sensitivity.

26    The HPS experiment [11] is preparing for installa-  
27   tion in Hall-B at JLab in the Fall of 2014. It searches  
28   for electro-produced  $A'$  in interactions between elec-  
29   trons and nuclei in a thin (0.25% R.L.) Tungsten target  
30   foil. The electrons are supplied by the nearly contin-  
31   uous JLab CEBAF beam with energy between 2.2 and  
32   6.6 GeV. The HPS experiment uses both invariant mass  
33   and secondary vertex signatures to search for  $A'$  decay-  
34   ing into  $e^+e^-$  pairs. In the interesting mass and coupling  
35   range, the decay products are boosted along the beam  
36   axis with small opening angles and decay lengths rang-  
37   ing from mm’s to tens of cm’s requiring HPS to operate  
38   tracking detectors down to 15 mrad opening angle only  
39   10 cm behind the target. HPS employs a  $\approx 1 \text{ m}$  long  
40   silicon tracking and vertexing detector inside a dipole  
41   magnet to measure charged particle trajectories and find  
42   the decay vertex position of oppositely charged pairs. A  
43   fast electromagnetic calorimeter sits just downstream of  
44   the magnet to provide a trigger and identify electrons.  
45   To overcome the background occupancy from multiple  
46   scattered beam electrons both detectors have excellent  
47   timing resolution and the experiment utilizes very high-  
48   rate front-end electronics. HPS is designed to run at

49    high trigger and data throughput rates in order to ex-  
50   ploit the 499 MHz bunch structure, 100% duty cycle, of  
51   the JLab CEBAF accelerator to accumulate the needed  
52   statistics.

53    The HPS Test Run, using a simplified version of the  
54   HPS apparatus, was proposed and approved at JLab as  
55   the first stage of HPS. Its purposes included demonstra-  
56   ting that the apparatus and data acquisition systems are  
57   technically feasible and the trigger rates and occupan-  
58   cies to be encountered in electron-beam running are as  
59   simulated. Given dedicated running time with electron  
60   beams, the HPS Test Run apparatus is capable of search-  
61   ing for heavy photons in unexplored regions of param-  
62   eter space. Therefore, key design criteria and require-  
63   ments for HPS and the HPS Test Run apparatus are the  
64   same:

- 65    • uniform acceptance between 15 and  $\approx 70$  mrad in  
66    the forward region to catch boosted decay products  
67    close to the beam,
- 68    • beam passage through the apparatus in vacuum, to  
69    eliminate direct interactions with the detector and  
70    minimize beam gas interactions,
- 71    • detector components that can survive and effi-  
72    ciently operate in a high radiation environment  
73    with local doses exceeding 100 Mrad,
- 74    • high-rate electronics with trigger rates up to  
75    50 kHz and data handling rates of 100 MB/s to per-  
76    manent storage,
- 77    • a flexible, redundant and efficient trigger selecting  
78    electron and positron pairs at rates up to 50 kHz,
- 79    • hit reconstruction efficiency higher than 99% and  
80    average track reconstruction efficiency higher than  
81    98% for electrons and positrons,
- 82    • excellent hit time resolution to reject out-of-time  
83    background hits in the nearly continuous CEBAF  
84    beam; 2 ns for hits on tracks in a 8 ns trigger win-  
85    dow,
- 86    • momentum and angular resolution better than  
87    4.5% and 1 to 4 mrad (across the track momen-  
88    tum range in non-bend direction), respectively, to  
89    reach  $A'$  mass resolution of 2.5% or less across the  
90    interesting mass range,
- 91    • resolution of distance of closest approach to the  
92    beam axis less than 250 (100)  $\mu\text{m}$  for tracks with  
93    0.5 (1.7)  $\text{GeV}/c$  momentum to achieve a Gaussian  
94    vertex resolution down to 1 mm at high masses

---

\*Corresponding author.

Email address: phansson@slac.stanford.edu (P. Hansson  
Adrian)

95 to discriminate displaced  $A'$  decays from prompt  
96 QED backgrounds,

97 The HPS Test Run apparatus was installed on April  
98 19, 2012, and ran parasitically in the photon beam of  
99 the HDice experiment [12] until May 18. The JLab run  
100 schedule precluded any dedicated electron beam run-  
101 ning, but the HPS Test Run was allowed a short ( $\approx$ 6h)  
102 and valuable dedicated photon beam run at the end of  
103 scheduled CEBAF running. During this dedicated pe-  
104 riod,  $e^+e^-$  pairs, produced in a gold foil upstream of the  
105 experiment, were studied. This dedicated running pro-  
106 vided valuable data to demonstrate the functionality of  
107 the apparatus, document its performance, and explore  
108 trigger rates, as shown below.

109 This paper reviews the HPS Test Run apparatus, doc-  
110 umenting the performance of the trigger, data acquisi-  
111 tion, silicon tracking and vertex detector, and the elec-  
112 tromagnetic calorimeter at, or close to, the level re-  
113 quired for calculating the physics reach of the HPS ex-  
114 periment.

## 115 2. Detector Overview

116 The HPS Test Run apparatus was designed to run  
117 in Hall B at JLab using the CEBAF 499MHz electron  
118 beam at energies between 2.2 and 6.6 GeV and cur-  
119 rents between 200 and 600 nA. The overall design of  
120 the experiment follows from the kinematics of  $A'$  pro-  
121 duction which typically results in a final state particle  
122 within a few degrees of the incoming beam, especially  
123 at low  $m_{A'}$ . Detectors must therefore be placed close  
124 to the beam. The intense electron beam enlarges down-  
125 stream after multiple scattering in the target and elec-  
126 trons which have radiated in the target disperse horizon-  
127 tally in the field of the analyzing magnet. Together they  
128 constitute a “wall of flame” which must be completely  
129 avoided. Accordingly, the apparatus is split vertically  
130 to avoid a “dead zone”, the region within  $\pm 15$  mrad of  
131 the beam plane. In addition, the beam is transported in  
132 vacuum through the tracker to minimize beam-gas inter-  
133 action backgrounds. Even with these precautions, the  
134 occupancies of sensors near the beam plane are high,  
135 dominated by the multiple Coulomb scattering of the  
136 primary beam, so high-rate detectors, a fast trigger, and  
137 excellent time tagging are required to minimize their  
138 impact. The trigger comes from a highly-segmented  
139 lead-tungstate ( $PbWO_4$ ) crystal calorimeter located just  
140 downstream of the dipole magnet.

142 A rendering of the apparatus installed on the beam line  
143 is shown in Figure 1 and an overview of the coverage,  
144 segmentation and performance is given in Table 1.

145 The silicon tracking and vertexing detector for the  
146 HPS Test Run, or SVT, resides in a vacuum cham-  
147 ber inside the Pair Spectrometer (PS) dipole magnet in  
148 Hall B at JLab. The magnetic field strength was 0.5 T  
149 oriented vertically throughout the run. The SVT has  
150 five measurement stations, or “layers,” beginning 10 cm  
151 downstream of the target. Each layer comprises a pair  
152 of closely-spaced silicon microstrip sensors responsi-  
153 ble for measuring a single coordinate, or “view”. In-  
154 troduction of a small (50 or 100 mrad) stereo angle  
155 between the two sensors of each layer provides three-  
156 dimensional tracking and vertexing throughout the ac-  
157 ceptance of the detector. In order to accommodate the  
158 dead zone, the SVT is built in two halves that are ap-  
159 proximately mirror reflections of one another about the  
160 plane of the nominal electron beam. Each layer in one  
161 half is supported on a common support plate with inde-  
162 pendent cooling and readout.

163 The electromagnetic calorimeter (ECal) is also split  
164 into two halves. Each half of the ECal consists of  
165 221  $PbWO_4$  crystals arranged in rectangular formation.  
166 There are five rows with 46 modules in each row except  
167 the row closest to the beam plane which has 37. The  
168 light from each crystal is read out by an Avalanche Photo-  
169 diode (APD) glued on the back surface of the crys-  
170 tal. Signals from the APDs are amplified using custom-  
171 made amplifier boards before being sent to the data ac-  
172 quisition electronics.

173 The Data Acquisition system combines two architec-  
174 tures, the Advanced Telecom Communications Archi-  
175 tecture (ATCA) based SVT readout system and VME-  
176 bus Switched Serial (VXS) based digitization and trig-  
177 gering system for the ECal.

## 178 3. The HPS Test Run Beamline

179 Since an electron beam was unavailable, the HPS Test  
180 Run detected the electrons and positrons produced by  
181 interactions of the secondary photon beam with a thin  
182 foil just upstream of the detectors. The HPS Test Run  
183 studied the performance of the detectors and the mul-  
184 tiple coulomb scattering of the electrons and positrons.  
185 Figure 2 shows the layout of the setup on the beam line.  
186 The SVT was installed inside the Hall B pair spectrom-  
187 eter magnet vacuum chamber with the ECal mounted  
188 downstream of it. Both the SVT and the ECal were re-  
189 tracted off the beam plane compared to nominal electron  
190 beam running to allow clean passage of the photon beam  
191 through the system.

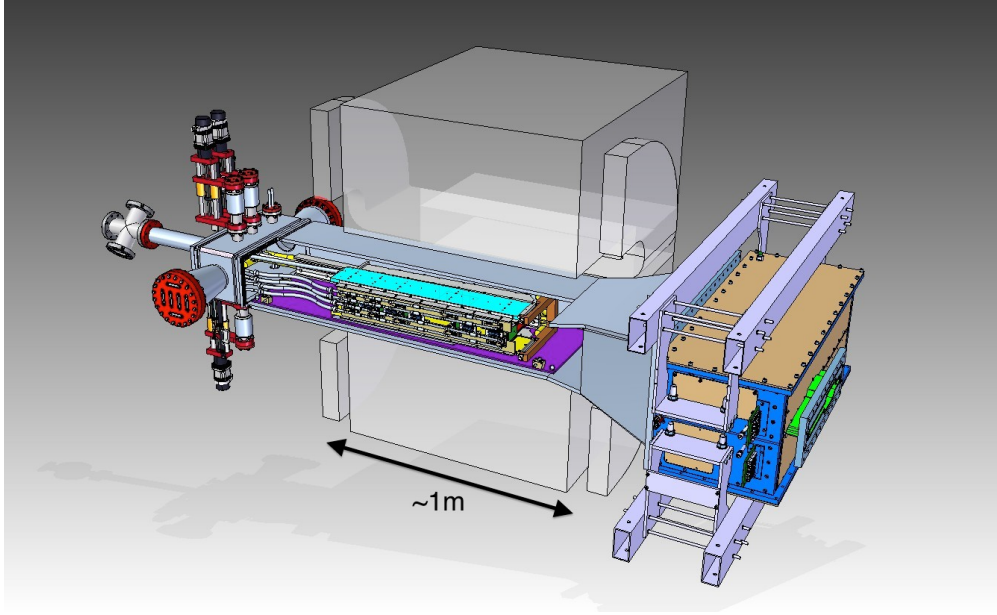


Figure 1: Rendering of the HPS Test Run apparatus installed on the beam line.

Table 1: Overview of the coverage, segmentation and performance of the HPS Test Run detector. The  $\sigma_{d_0}$  is the track impact parameter resolution of the SVT at the nominal electron target position.  $\sigma_{pos}$  is the estimated position resolution perpendicular to the strip direction on the silicon sensors of the SVT.

| System | Coverage (mrad)                  | # channels | ADC (bit) | # layers             | Segmentation                                                                                       | Time resolution (ns) | Performance                                                                                                                |
|--------|----------------------------------|------------|-----------|----------------------|----------------------------------------------------------------------------------------------------|----------------------|----------------------------------------------------------------------------------------------------------------------------|
| SVT    | $15 < \theta_y < 70$<br>(5 hits) | 12780      | 14        | 5<br>(stereo layers) | $30 \mu\text{m}$ (sense)<br>$60 \mu\text{m}$ (readout)<br>( $\sigma_{pos} \approx 6 \mu\text{m}$ ) | 2.5                  | $\sigma_{d0,y} \approx 100 \mu\text{m}$<br>$\sigma_{d0,x} \approx 300 \mu\text{m}$<br>$\sigma_{d0,z} \approx 1 \text{ mm}$ |
| ECal   | $15 < \theta_y < 60$             | 442        | 12        | 1                    | $1.33 \times 1.33 \text{ cm}^2$<br>$1.6 \times 1.6 \text{ cm}^2$                                   | 4<br>(trigger)       | $\sigma(E)/E \approx 4.5\%/\sqrt{E}$<br>Ref. [13, 14, 15]                                                                  |

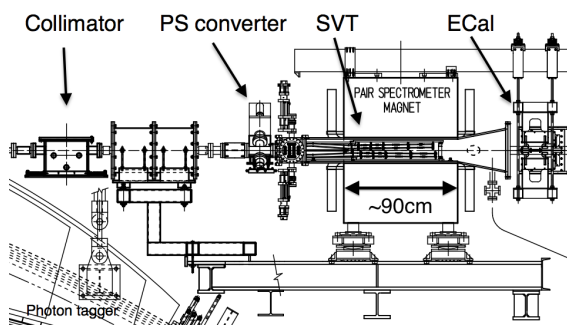


Figure 2: Layout of the HPS parasitic run.

The photon beam was generated in the interaction of 5.5 GeV electrons with a  $10^{-4} X_0$  gold radiator located  $\approx 9$  m upstream of the PS. The primary beam and scattered electrons are deflected away from detectors by the dipole magnet of the photon tagging system. During the dedicated HPS Test Run period, the collimated (6.4 mm diameter) photon beam passes through the PS pair converter gold foil and later the HPS system. The PS pair converter was located  $\approx 77$  cm upstream of the first layer of the SVT.

Data was taken on three different converter thicknesses with photon fluxes between 0.4 and  $1.3 \times 10^8/\text{s}$  at photon energies between 0.55 and 5.5 GeV produced by a 30 to 90 nA electron beam. Data was measured for both polarities of the PS dipole magnet. The photon beam line during the HPS Test Run produced a relatively large number of  $e^+e^-$  pairs originating upstream

| Converter thickn.<br>(% $X_0$ ) | Duration<br>(s) | $e^-$ on radiator<br>( $\mu\text{C}$ ) |
|---------------------------------|-----------------|----------------------------------------|
| 0                               | 1279            | 88.1                                   |
| 0.18                            | 2640            | 193.5                                  |
| 0.45                            | 2149            | 140.7                                  |
| 1.6                             | 911             | 24.4                                   |

Table 2: Measured integrated currents for the dedicated photon runs.

of the converter position. This contribution was measured during data taking with “empty” converter runs, i.e. removing the converter but with all other conditions the same. The runs taken during the time dedicated to HPS Test Run are summarized in Table 2.

#### 4. Silicon Vertex Tracker

The Silicon Vertex Tracker (SVT) enables efficient reconstruction of charged particles and precise determination of their trajectories. This allows  $A'$  decays to be distinguished from background via simultaneous measurements of the invariant mass of  $e^+e^-$  decay products and the position of decay vertices downstream of the target.

The design of the SVT is primarily driven by physics requirements and constraints from the environment at the interaction region. The  $A'$  decay products have momenta in the range of 0.4-2.0 GeV/c (from a 2.2 GeV beam), so multiple scattering dominates mass and vertexing uncertainties for any possible material budget. The SVT must therefore minimize the amount of material in the tracking volume. The signal yield for long-lived  $A'$  is very small, so the rejection of prompt vertices must be exceedingly pure, on the order of  $10^{-7}$ , in order to eliminate all prompt backgrounds. To achieve the required vertexing performance the first layer of the SVT must be placed no more than about 10 cm downstream of the target. At that distance, it is found that the active region of a sensor can be placed as close as 1.5 mm from the center of the beam, defining the 15 mrad “dead zone” mentioned previously, to maximize low-mass  $A'$  acceptance with decay products nearly collinear with the beam axis. At the edge of this “dead zone”, the radiation dose approaches  $10^{15}$  electrons/cm<sup>2</sup>/month, or roughly  $3 \times 10^{14}$  1 MeV neutron equivalent/cm<sup>2</sup>/month [16], requiring the sensors to be actively cooled. Meanwhile, very low-energy delta rays from beam-gas interactions would multiply the density of background hits, so the SVT must operate inside the beam vacuum. Finally, in order to protect the sensors, the detector must be movable

so that it can be retracted during periods of uncertain beam conditions or beam tuning.

Good mass resolution is needed across the interesting mass range to discover the  $A'$  signal on top of the copious QED background in the bump-hunt search. Track momentum and angular resolution of 4-5% and 1-4 mrad (across the momentum range in the non-bend plane which dominates the measurement), respectively, translates into a 2.5% mass resolution for  $A'$  decay opening angles between 15-70 mrad [11]. With multiple scattering dominating both mass and vertexing uncertainties, spatial hit resolution less than 50  $\mu\text{m}$  are required in the non-bend plane in the first few layers which dominates the vertexing performance and about twice that in the non-bend plane.

High background occupancies, up to 4 MHz/mm<sup>2</sup> locally, in the region closest to the beam result from beam electrons undergoing multiple scattering in the target. These background hits are rejected by requiring the time reconstruction of each hit to be better than 2 ns.

##### 4.1. Layout

The layout of the SVT is summarized in Table 3 and rendered in Figure 3. Each of the layers is comprised of a pair of closely-spaced silicon microstrip sensors mounted back-to-back to form a module. A 100 mrad stereo angle is used in the first three layers to provide higher-resolution 3D space points for vertexing. Using 50 mrad in the last two layers breaks the tracking degeneracy of having five identical layers and minimizes fakes from ghost hits to improve pattern recognition. Altogether, the SVT has 20 sensors for a total of 12780 readout channels.

| Layer                           | 1            | 2            | 3            | 4             | 5             |
|---------------------------------|--------------|--------------|--------------|---------------|---------------|
| $z$ from target (cm)            | 10           | 20           | 30           | 50            | 70            |
| Stereo angle (mrad)             | 100          | 100          | 100          | 50            | 50            |
| Bend res. ( $\mu\text{m}$ )     | $\approx 60$ | $\approx 60$ | $\approx 60$ | $\approx 120$ | $\approx 120$ |
| Non-bend res. ( $\mu\text{m}$ ) | $\approx 6$  | $\approx 6$  | $\approx 6$  | $\approx 6$   | $\approx 6$   |
| # of sensors                    | 4            | 4            | 4            | 4             | 4             |
| Dead zone (mm)                  | $\pm 1.5$    | $\pm 3.0$    | $\pm 4.5$    | $\pm 7.5$     | $\pm 10.5$    |
| Power cons. (W)                 | 6.9          | 6.9          | 6.9          | 6.9           | 6.9           |

Table 3: Layout of the SVT.

The SVT is built in two separate halves that are mirror reflections of one another about the plane of the nominal electron beam. Each half consists of five modules mounted on a support plate that provides services to the

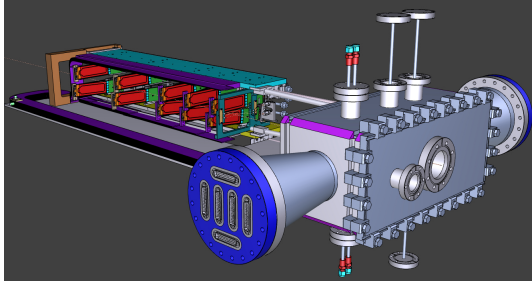


Figure 3: A rendering of the SVT showing the modules on their support plates held by the hinged C-support on the left and the motion levers on the right. The sensors are shown in red and the hybrid readout boards in green. The beam enters from the right through a vacuum box with flanges for services.

modules and allows them to be moved as a group relative to the dead zone. The two halves of the tracker are connected to hinges mounted on a C-shaped support just beyond the last layer that defines the nominal spacing between the upper and lower halves of the tracker. A shaft attached to each support plate in front of layer one extends upstream and connects to a linear shift that transfers motion into the vacuum box through bellows to open and close the two halves around the dead zone. The C-support is mounted to an aluminum baseplate that defines the position of the SVT with respect to the vacuum chamber. Figure 4 shows a photograph of both completed detector halves prior to final assembly.



Figure 4: Both halves of the HPS Test Run SVT after final assembly at SLAC. The cooling manifolds and integrated cable runs are clearly seen.

299

#### 300 4.2. Components

301 The sensors for the SVT are  $p+$ -on- $n$ , single-sided,  
302 AC-coupled, polysilicon-biased microstrip sensors fab-  
303 ricated on  $<100>$  silicon and have 30 (60)  $\mu\text{m}$  sense

304 (readout) pitch over their  $4 \times 10 \text{ cm}^2$  surface. This  
305 sensor technology was selected to match the require-  
306 ment of  $< 1\% X_0$  per layer, single-hit resolution bet-  
307 ter than 50  $\mu\text{m}$  and tolerance of a radiation dose of ap-  
308 proximately  $1.5 \times 10^{14}$  1 MeV neutron equivalent/ $\text{cm}^2$   
309 for a six month run. The sensors, produced by Ham-  
310 matsu Photonics Corporation, were originally meant  
311 for the cancelled Run 2b upgrade of the DØ exper-  
312 iment [17] which satisfied the requirement that the  
313 technology must be mature and available within the time and  
314 budget constraints.

315 Despite having only small spots with very high occu-  
316 pancy (up to  $4 \text{ MHz/mm}^2$ ) closest to the primary beam,  
317 the rates are still high and lowering the peak occupancy  
318 to approximately 1% for tracking requires a trigger win-  
319 dows and hit time tagging of roughly 8 ns. The ECal  
320 readout and trigger described in Sec. 5.3 can achieve  
321 such resolution. To reach this performance the sen-  
322 sors for the SVT are readout by the APV25 ASIC de-  
323 veloped for the CMS experiment at CERN [18]. The  
324 APV25 can capture successive samples of the shaper  
325 output in groups of three at a sampling rate of approx-  
326 imately 40 MHz. By fitting the known  $CR-RC$  shaping  
327 curve to these samples, the initial time of the hit can  
328 be determined to a precision of 2 ns for  $S/N \approx 25$  [19].  
329 For electron beam running, six-sample readout and the  
330 shortest possible shaping time (35 ns) is used to best  
331 distinguish hits that overlap in time. The APV25 ASICs  
332 are hosted on simple FR4 hybrid readout boards, out-  
333 side the tracking volume, with a short twisted-pair pig-  
334 tail cable to provide power and configuration and signal  
335 readout. Along with a single sensor, these are glued  
336 to a polyimide-laminated carbon fiber composite back-  
337 ing making up a half-module. A window is machined  
338 in the carbon fiber leaving only a frame around the pe-  
339 riphery of the silicon to minimize material. A 50  $\mu\text{m}$   
340 sheet of polyamide is laminated to the surface of the  
341 carbon fiber with 1 mm overhang at all openings to en-  
342 sure good isolation between the back side of the sensor,  
343 carrying high-voltage bias, and the carbon fiber which  
344 is held near ground.

345 The sensor modules for the SVT consist of a pair  
346 of identical half-modules, sandwiched back-to-back  
347 around an aluminum cooling block at one end and a sim-  
348 ilar PEEK spacer block at the other. Figure 5 shows a  
349 single module after assembly. The cooling block pro-  
350 vides the primary mechanical support for the module as  
351 well as cooling via copper tubes pressed into grooves  
352 in the plates. The spacer block defines the spacing be-  
353 tween the sensors at the far end of the module, stiffens  
354 the module structure, and improves the stability of the  
355 sensor alignment. The average support material in the

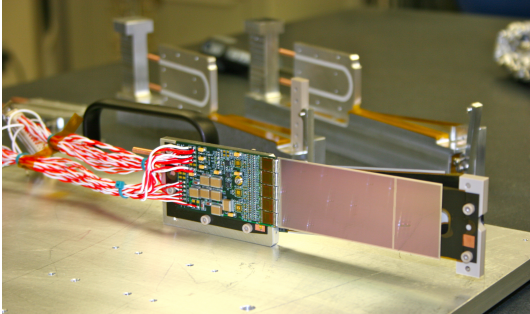


Figure 5: A prototype module assembly (foreground) with the 50 mrad (left) and 100 mrad (right) module assembly fixtures in the background. A pair of cooling blocks and a spacer block can be seen on the fixtures.

389 optical survey of individual modules with a precision of  
 390 a few  $\mu\text{m}$  was combined with a touch-probe survey of  
 391 the overall SVT support structure, with 25-100  $\mu\text{m}$  pre-  
 392 cision, to locate the silicon sensor layers with respect  
 393 to the support plates and the mechanical survey balls  
 394 on the base plate. After full assembly and installation  
 395 of the SVT at JLab, a mechanical survey of the SVT  
 396 base plate position inside the pair spectrometer vacuum  
 397 chamber is used to determine the global position of the  
 398 SVT with respect to the CEBAF beam line. The re-  
 399 sulting survey-based alignment has the position of the  
 400 silicon sensors correct to within a few hundred microns  
 401 measured from tracks in the HPS Test Run data. A more  
 402 sophisticated global track-based alignment technique to  
 403 reach final alignment precision well below 50  $\mu\text{m}$  is be-  
 404 ing developed.

356 tracking volume is approximately 0.06%  $X_0$  per double-  
 357 sided module for a total material budget of 0.7% per  
 358 layer.

359 The total SVT power consumption budget of about  
 360 50 W is removed by a water/glycol mixture circulated  
 361 through a flexible manifold attached to the copper tubes  
 362 in the cooling blocks. During the HPS Test Run the  
 363 sensors were operated at around 23° C. The power con-  
 364 sumption is dominated by five APV25 ASICs on each  
 365 hybrid board consuming approximately 2 W, radiant  
 366 heat load is less than 0.5 W per sensor and leakage cur-  
 367 rent is only significant in a small spot after irradiation.

#### 368 4.3. Production, Assembly and Shipping

369 Hybrids with APV25 ASICs underwent quick qualifi-  
 370 cation testing and each half-module was run at low tem-  
 371 perature ( $\approx 5^\circ \text{C}$ ) and fully characterized for pedestals,  
 372 gains, noise and time response after assembly. Of 29  
 373 half-modules built, 28 passed qualification testing, leav-  
 374 ing eight spare modules after completion of the SVT.  
 375 Only sensors capable of 1000 V bias voltage without  
 376 breakdown were used. Full-module assembly and me-  
 377 chanical surveys were performed at SLAC before final  
 378 assembly, testing and shipping of the SVT to JLab. A  
 379 custom shipping container with nested crates and redun-  
 380 dant isolation for shock and vibration was built in or-  
 381 der to safely send the partly assembled SVT to JLab.  
 382 At JLab, the entire SVT was integrated with the full  
 383 DAQ and the power supplies before moving the module-  
 384 loaded support plates to Hall B for final mechanical as-  
 385 sembly and installation inside of the vacuum chamber.

#### 386 4.4. Alignment

387 The SVT was aligned using a combination of optical,  
 388 laser and touch probe surveys at SLAC and JLab. The

## 5. Electromagnetic Calorimeter

406 The electromagnetic calorimeter (ECal), installed  
 407 downstream of the PS dipole magnet, performs two es-  
 408 sential functions for the experiment: it provides a trigger  
 409 signal to select what events to read out from the detector  
 410 sub-systems and is used in the analysis to identify elec-  
 411 trons and positrons. The technology and design choices  
 412 are largely driven by the need for a compact forward de-  
 413 sign covering the SVT A' acceptance and able to fully  
 414 absorb electrons and positrons with energy between 0.5-  
 415 6.5 GeV. It needs granularity and signal readout speed  
 416 to handle 1 MHz/cm<sup>2</sup> of electromagnetic background  
 417 and to be radiation hard. While the trigger for A' events  
 418 is largely insensitive to the energy resolution, in order  
 419 to have the possibility to improve the energy resolu-  
 420 tion from the SVT measurement  $\sigma(E)/E < 4.5\%/\sqrt{E}$  is  
 421 needed.

422 The PbWO<sub>4</sub> crystal inner calorimeter of the CLAS  
 423 detector [13, 14, 15], in operation since 2005 in Hall  
 424 B, meets all the requirements set by HPS. The mod-  
 425 ules from this calorimeter have been subsequently re-  
 426 purposed for HPS.

### 427 5.1. Components

428 The ECal module shown in Figure 6 is based on a  
 429 tapered 160 mm long PbWO<sub>4</sub> crystal with a 13.3  $\times$   
 430 13.3 mm<sup>2</sup> (16  $\times$  16 mm<sup>2</sup>) front (rear) face wrapped in  
 431 VM2000 multilayer polymer mirror film. The scin-  
 432 tillation light yield, approximately 120 photons/MeV,  
 433 is read out by a 5 $\times$ 5 mm<sup>2</sup> Hamamatsu S8664-55  
 434 Avalanche Photodiode (APD) with 75% quantum effi-  
 435 ciency glued to the rear face surface using MeltMount  
 436 1.7 thermal plastic adhesive. This results in about 8

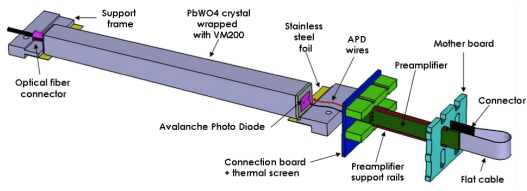


Figure 6: A schematic view of an ECal module.

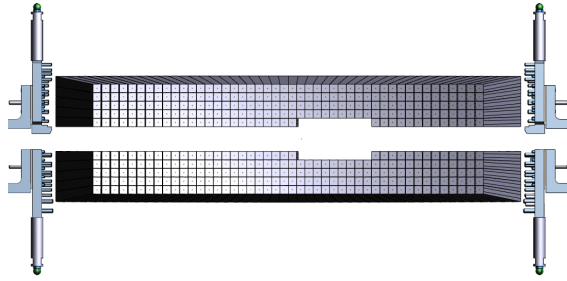


Figure 7: Rendered layout view of the ECal looking downstream.

437 photoelectrons/MeV which needs to be amplified before  
 438 fed into the FADC for digitization and processing. The  
 439 maximum energy deposited in a crystal is expected to  
 440 be 4.2 GeV which needs to match the input range of the  
 441 FADC. The relatively low gain of the APD ( $\sim 200$ ) was  
 442 compensated with custom-made preamplifier boards,  
 443 that provide further amplification to match the 2 V dy-  
 444 namic range of the FADC. With a total noise level of  
 445 about 10 MeV and a resolution of about 1 ADC/MeV  
 446 the ADC resolution fulfills the requirements from HPS.

### 447 5.2. Layout

448 Similar to the SVT, the ECal is built in two separate  
 449 halves that are mirror reflections of one another about  
 450 the plane of the nominal electron beam to avoid inter-  
 451 fering with the 15 mrad “dead zone”. As shown in Fig-  
 452 ure 7, the 221 modules in each half, supported by alu-  
 453 minum support frames, are arranged in rectangular for-  
 454 mation with five layers and 46 crystals/layer except for  
 455 the layer closest to the beam where nine modules were  
 456 removed to allow a larger opening for the outgoing elec-  
 457 tron and photon beams. Each half was enclosed in a  
 458 temperature controlled box ( $< 1^\circ \text{ F}$  stability and  $< 4^\circ \text{ F}$   
 459 uniformity) to stabilize the crystal light yield and the op-  
 460 eration of the APDs and its preamplifiers. Four printed  
 461 circuit boards mounted on the backplane penetrated the  
 462 enclosure and were used to supply the  $\pm 5$  V operating  
 463 voltage for the preamplifiers, 400 V bias voltage to the  
 464 APDs, and to read out signals from the APDs. Each half  
 465 of the ECal was divided into 12 bias voltage groups with  
 466 a gain uniformity of about 20%.

467 During the HPS Test Run, both halves were held in  
 468 place by four vertical bars attached to a rail above, plac-  
 469 ing the front face of the crystals 147 cm from the up-  
 470 stream edge of the magnet, with a 8.7 cm gap between  
 471 the innermost edge of the crystals in the two halves.

### 472 5.3. Signal readout

473 After a 2:1 signal splitter, 1/3 of an amplified APD  
 474 signal was fed to a single channel of a JLab flash ADC  
 475 (FADC) board [20]. 2/3 of the signal was sent to a

476 discriminator module and then to a TDC for a timing  
 477 measurement. The FADC boards are high speed VXS  
 478 modules digitizing up to 16 APD signals at 250 MHz  
 479 and storing samples in 8  $\mu\text{s}$  deep pipelines with 12-bit  
 480 resolution. When a trigger is received, the part of the  
 481 pipeline from 5 samples before and 30 after the signal  
 482 which crossed a programmable threshold (for the HPS  
 483 Test Run this was set to  $\approx 70$  MeV) are summed and  
 484 stored in a 17-bit register for readout. In addition a  
 485 4 ns resolution timestamp of the threshold crossing is  
 486 reported in the readout for each pulse. This scheme  
 487 significantly compresses the data output of the FADC.  
 488 During offline data analysis, a calibrated pedestal value  
 489 is subtracted to obtain the actual summed energy. Two  
 490 20-slot VXS crates with 14 (13) FADC boards were em-  
 491 ployed in the HPS Test Run to read out the top (bottom)  
 492 half of the ECal.

## 493 6. Trigger and Data Acquisition

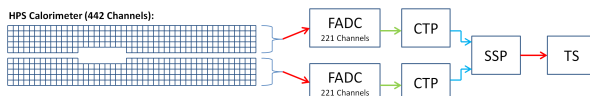
494 The DAQ system handles acquisition of data from the  
 495 ECal and SVT sub-detectors with two DAQ architec-  
 496 tures. The SVT DAQ is based on Advanced Telecom  
 497 Communications Architecture (ATCA) hardware while  
 498 the ECal uses VMEbus Switched Serial (VXS) based  
 499 hardware. Data from the sub-detectors are only read  
 500 out when a trigger signal from the trigger system is re-  
 501 ceived.

### 502 6.1. Trigger system

503 The trigger system is designed to select time coinci-  
 504 dences of electromagnetic clusters in the top and bot-  
 505 tom halves of the ECal satisfying loose kinematic se-  
 506 lections optimized on simulated  $A'$  events to further re-  
 507 duce the rate. The trigger system need to be essentially  
 508 dead time free, handle rates up to 50 kHz and impor-  
 509 tantly supply a trigger time relative to the beam bunches

510 with 8 ns to reduce the background from out-of-time  
 511 hits in the high occupancy regions of the SVT. Figure 8  
 512 shows a schematic overview of each stage of the system.  
 513 Each channel on the FADC board has an independent data path to send 5-bit pulse energy and 3-bit pulse  
 514 arrival time information every 32 ns to a trigger processing board (CTP), which is in the same crate. The  
 515 3-bit pulse arrival time allows the trigger to know the  
 516 pulse timing at 4 ns resolution. Contrary to the read-  
 517 out path described in Sec. 5.3, this energy is a pedestal-  
 518 subtracted time-over-threshold sum with programmable  
 519 offsets and minimum threshold discriminator for each  
 520 channel. With input from all FADC channels, i.e. one  
 521 half of the ECal, the CTP performs cluster finding and  
 522 calculates cluster energy and timing information. The  
 523 3x3 fixed-window, highly parallel, FPGA-based cluster  
 524 algorithm simultaneously searches for up to 125 clusters  
 525 with energy sum larger than the programmable energy  
 526 threshold ( $\approx$  270 MeV). Crystals in the fixed-window  
 527 are included in the sum if the leading edge of the pulse  
 528 occurred within a 32 ns time window to take into ac-  
 529 count clock skew and jitter throughout the system. The  
 530 CTP only accepts clusters with the locally highest en-  
 531 ergy 3x3 window to deal with overlapping and very  
 532 large clusters. The sub-system board (SSP) receives the  
 533 clusters from the top and bottom half CTP at a max-  
 534 imum of 250MHz and searches for pairs of clusters in  
 535 an 8 ns wide coincidence window. The SSP sends trig-  
 536 gers to the trigger supervisor (TS), which generates all  
 537 the necessary signals and controls the entire DAQ sys-  
 538 tem readout through the trigger interface units installed  
 539 in every crate that participate in the readout process.  
 540

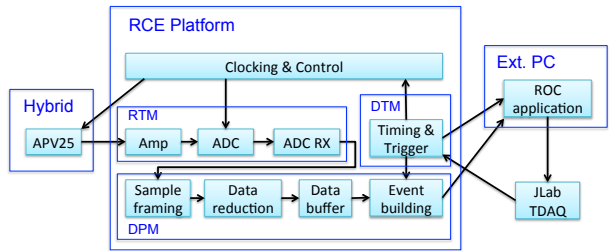
541 The trigger system is free-running and driven by the  
 542 250 MHz global clock and has essentially zero dead  
 543 time at the occupancies expected for HPS. The trigger  
 544 supervisor can apply dead time if necessary, for example  
 545 on a ‘busy’ or ‘full’ condition from the front-end elec-  
 546 tronics. The system is designed to handle trigger rates  
 547



548 Figure 8: Block diagram of the ECAL trigger system consisting  
 549 of the FADC that samples and digitizes signals for each detector  
 550 channel and sends them for cluster finding in the CTP. The  
 551 CTP clusters are sent to the SSP where the final trigger de-  
 552 cision is taken based on pairs of clusters in both halves of the  
 553 ECal. The decision is sent to the Trigger Supervisor (TS) that  
 554 generates the necessary signals to read out the sub-detectors.  
 555



556 Figure 9: The SVT DAQ COB board with four data processing  
 557 daughter cards (DPMs) visible on the left side.  
 558



559 Figure 10: Block diagram overview of the SVT DAQ.  
 560

561 above 50 kHz and has a latency set to  $\approx 3 \mu\text{s}$  to match  
 562 that required by the SVT APV25 ASIC.  
 563

564 During the HPS Test Run, for the most part the trigger  
 565 system required only a single cluster in either the top or  
 566 bottom ECal halves but was tested to trigger rates above  
 567 100 kHz by lowering thresholds.  
 568

## 6.2. SVT Data Acquisition

569 The purpose of the SVT DAQ is to support the con-  
 570 tinuous 40 MHz readout and processing of signals from  
 571 each of the 20 silicon strip sensors of the SVT. The data  
 572 for each strip channel, six samples of the signal, needs  
 573 to be transferred to the JLab DAQ for those events se-  
 574 lected by the trigger at rates up to 50 kHz and with data  
 575 transfer rates up to 100 MB/s.  
 576

577 The SVT DAQ is based on the Reconfigurable Clus-  
 578 ter Element (RCE) and cluster interconnect concept de-  
 579 veloped at SLAC as generic building blocks for DAQ  
 580 systems. The RCE is a generic computational build-  
 581 ing block, housed on a separate daughter card called  
 582 Data Processing Module (DPM), that is realized on an  
 583 ATCA front board called the Cluster On Board (COB),  
 584 see Figure 9. The first generation RCE used in the HPS  
 585 Test Run consisted of a Virtex 5 FPGA with 1 GB of  
 586 DDR3 RAM. A schematic overview of the system is  
 587 shown in Figure 10. The analog outputs of up to 12  
 588

573 SVT half-modules (60 APV25 ASICs) are digitized on 622  
574 the Rear-Transition-Module (RTM), a custom board on 623  
575 the back side of the ATCA crate, interfacing the HPS- 624  
576 specific readout to the generic DAQ components on the 625  
577 COB. A pre-amplifier converts the APV25 differential 626  
578 current output to a different voltage output scaled to the 627  
579 sensitive range of a 14-bit ADC operating at the system 628  
580 clock of 41.667 MHz. The RTM is organized into four 629  
581 sections with each section supporting three SVT half- 630  
582 module hybrids (15 APV25 ASICs). The RTM also 631  
583 includes a 4-channel fiber-optic module and supporting 632  
584 logic which is used to interface to the JLab trigger 633  
585 system supervisor. Each section of the RTM is input to a 634  
586 DPM which apply thresholds for data reduction and 635  
587 organizes the sample data into UDP datagrams. The DPM 636  
588 also hosts an I<sup>2</sup>C controller used to configure and mon- 637  
589 itor the APV25 ASICs. A single ATCA crate with two 638  
590 COB cards was used, one supporting four DPMs and 639  
591 one supporting three DPMs and one DPM that is con-  
592 figured as the trigger and data transmission module. The  
593 two COB cards and their DPMs are interconnected with  
594 a 10 Gb/s switch card [21] which also hosts two 1Gb/s  
595 Ethernet interfaces to the external SVT DAQ PC.

596 The external PC supports three network interfaces:  
597 two standard 1 Gb/s Ethernet and one custom low-  
598 latency data reception card. The first is used for slow  
599 control and monitoring of the 8 DPM modules and the  
600 second serves as the interface to the JLAB data acquisi-  
601 tion system. The third custom low-latency network in-  
602 terface is used to receive data from the ATCA crate and  
603 supports a low latency, reliable TTL trigger acknowl-  
604 edge interface to the trigger DPM. This PC hosts the  
605 SVT control and monitoring software as well as the  
606 Read Out Controller application used to interface with  
607 the JLab DAQ.

608 In order to minimize cable length for the analog  
609 APV25 output signal the ATCA crate was located ap-  
610 proximately 1 m from the beam line, next to our ca-  
611 ble vacuum feed-throughs. Before shielding with lead-  
612 blankets was arranged, we observed two failures of  
613 normally reliable ATCA crate power supplies, time-  
614 correlated to beam instabilities.

615 Although trigger rates during the HPS Test Run were  
616 significantly lower, this system was tested at trigger  
617 rates up to 20 kHz and 50 MB/s. With optimized event  
618 blocking and improved ethernet bandwidth, together  
619 with utilizing the overlapping readout and trigger func-  
620 tionality of the APV25, the system is capable of being  
621 read out at 50 kHz trigger rate.

### 6.3. General Data Acquisition and Online Computing

Every crate participating in the readout process contains a Readout Controller (ROC) that collects digitized information, processes it, and sends it on to the event builder. For the ECal, both VXS crates run ROC applications in a single blade Intel-based CPU module running CentOS Linux OS. For the SVT DAQ, the ROC application runs on the external PC under RHEL. The event builder assembles information from the ROCs into a single event which is passed to the event recorder that writes it to a RAID5-based data storage system capable of handling up to 100 MB/s. The event builder and other critical components run on multicore Intel-based multi-CPU servers. The DAQ network system is a network router providing 10 Gb/s high-speed connection to the JLab computing facility for long-term storage. For the HPS Test Run, both the SVT and ECal ROC had a 1 Gb/s link to the network router.

## 7. Reconstruction and Performance

While dedicated electron beam was precluded for the HPS Test Run the short dedicated photon beam run allowed the study of some of the key performance parameters for HPS and also explore the expected trigger rates during electron beam running. This section documents the performance and discusses the results implication for HPS.

### 7.1. SVT Performance

For the duration of the HPS Test Run all SVT modules and APV25 chips were configured to their nominal operating points [22] with all sensors reverse-biased at 180 V. The sensors were operated within a temperature range of 20 – 24°C. Approximately 97% of the 12,780 SVT channels were found to be operating normally; the fraction of dead or noisy channels varied from 2.4% to 4.7% throughout the HPS Test Run. Most of these losses were due to 2-4 misconfigured APV25 ASICs, a known noisy half-module and problems in two particular APV25 ASICs.

#### 7.1.1. Cluster and Hit Reconstruction

Track reconstruction in the SVT puts stringent requirement on the clustering and hit reconstruction. The multiple scattering in the tracking material dominates the uncertainty in the track parameter estimation and effectively determines the roughly 50 μm (200 μm) requirement on the spatial hit resolution in the non-bend (bend) plane. The high occupancy due to multiple scattered beam electrons in the target close to the beam requires a hit time resolution of 2 ns to efficiently reject

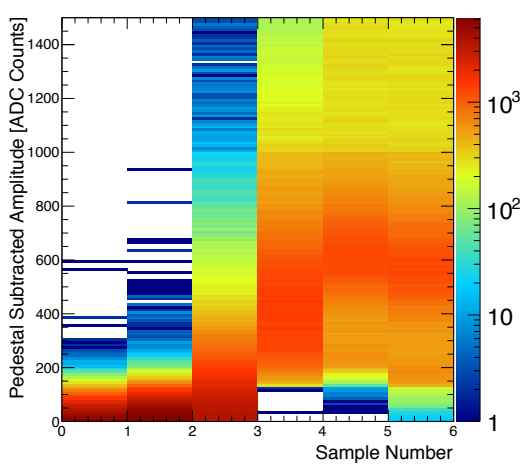


Figure 11: Accumulation of six pedestal-subtracted samples from individual SVT channels associated with hits on tracks.

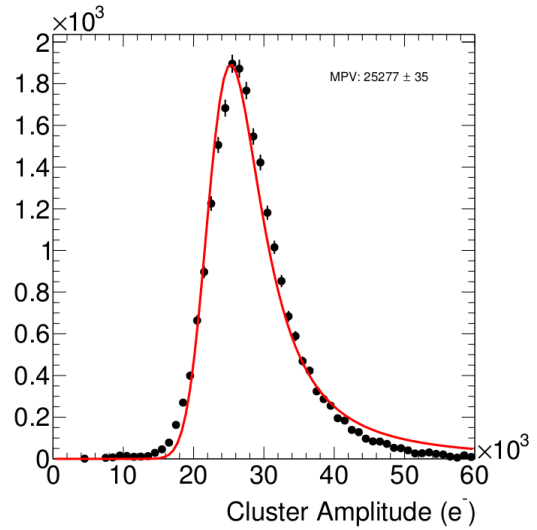


Figure 12: The cluster charge distribution for hits associated with a track follow the characteristic Landau shape.

670 out-of-time hits in HPS. Both the hit time, based on a  
 671 fit to the APV25 ASIC pulse shape, and the spatial po-  
 672 sition reconstruction rely on having S/N around 25 for  
 673 the sensors used in HPS.

674 After a trigger is received, the amplitude of every  
 675 APV25 analogue output is sampled and digitized in six  
 676 consecutive time bins, separated by roughly 25 ns. A  
 677 data reduction algorithm is applied requiring three out  
 678 of six samples to be above two times the noise level and  
 679 that the third sample is larger than the second or that  
 680 the fourth sample is larger than the third. The typical,  
 681 pedestal subtracted, pulse shape obtained is shown in  
 682 Figure 11. As the figure demonstrates, the SVT was  
 683 well timed-in to the trigger with the rise of the pulse  
 684 at the 3rd sampling point. In order to find the time,  $t_0$ ,  
 685 and amplitude of each hit, the six samples from each  
 686 channel are fitted to an ideal  $CR - RC$  function. Note  
 687 that in the HPS Test Run the APV25 ASICs were oper-  
 688 ating with a 50 ns shaping time. These hits are passed  
 689 through a simple clustering algorithm which forms clus-  
 690 ters by grouping adjacent strips with the position of  
 691 a cluster on the sensor determined by the amplitude-  
 692 weighted mean. With a linear gain up to  $\approx 3$  MIPs,  
 693 the cluster charge for hits associated with a track fol-  
 694 low the characteristic Landau shape, see Figure 12. A  
 695 noise level between  $1.1 - 1.5 \times 10^3$  electrons was estab-  
 696 lished through multiple calibration runs giving a signal  
 697 to noise ratio of  $21 - 25$ , in line with the requirement for  
 698 HPS. Radioactive source tests were used to provide the  
 699 absolute charge normalization. After clustering hits on

700 a sensor, the hit time for each cluster is computed as the  
 701 amplitude-weighted average of the individually fitted  $t_0$   
 702 on each channel. The  $t_0$  resolution is studied by com-  
 703 paring the cluster hit time with the average of all cluster  
 704 hit times on the track shown in Figure 13. After cor-  
 705 recting for offsets from each sensor (time-of-flight and  
 706 clock phase) and accounting for the correlation between  
 707 the  $t_0$  and track time, the extracted  $t_0$  resolution is 2.6 ns.  
 708 This is somewhat worse than the approximately 2 ns res-  
 709 olution expected for S/N=25 which we attribute to the  
 710 true pulse shape differing from our idealized fit function  
 711 which will be improved in the future [23]. Reducing the  
 712 APV25 ASIC pulse shaping time to 35 ns will also im-  
 713 prove time resolution. These results show that we can  
 714 operate with the six sample readout mode of the APV25  
 715 chip and achieve time resolution adequate for pileup re-  
 716 jection during electron running in HPS.

717 Good agreement was obtained between observed and  
 718 simulated occupancies after taking into account dead or  
 719 noisy channels. The hit reconstruction efficiency was  
 720 estimated by measuring the number of good tracks with  
 721 a hit close to the extrapolated intersection of a given  
 722 sensor that was excluded from the track fit itself. Tracks  
 723 which intersect regions with known bad channels or  
 724 pass very close to the edge region were excluded. The  
 725 hit reconstruction efficiency, see Figure 14, was mea-  
 726 sured to be above 98% and fairly uniform across the  
 727 SVT.

The spatial resolution of similar microstrip sensors is

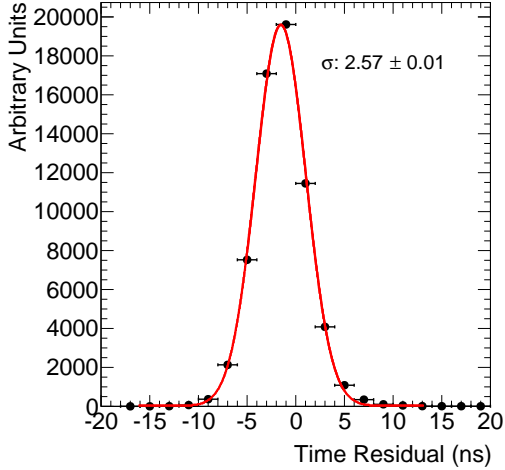


Figure 13: The residual of individual cluster times with the average of all clusters on the track.

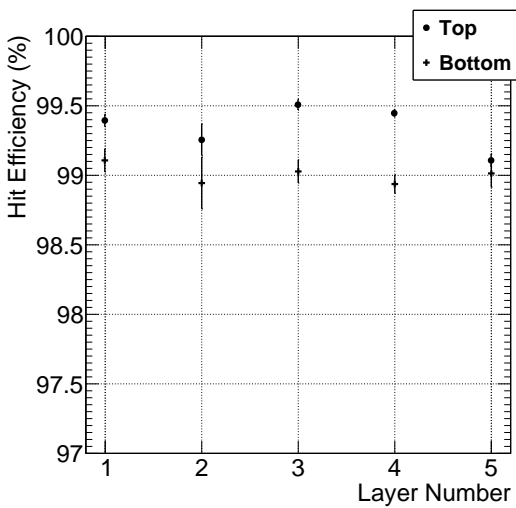


Figure 14: The hit reconstruction efficiency as a function of detector layer.

well established by test beam data, against which the charge deposition model in the simulation is validated. This resolution can be parameterized as a function of the total signal to single-strip noise and the crossing angle of tracks through the sensor. The single-hit resolution for charged particles with signal-to-noise ratio above 20, as demonstrated here, is relatively constant at approximately  $6 \mu\text{m}$  for tracks that enter approximately normal to the sensors as in HPS. This resolution is significantly better than the requirement for reaching the mass and vertex resolutions required for HPS.

#### 7.1.2. Momentum and Vertexing Resolution

Good track reconstruction performance is crucial to HPS. Simulations show that track momentum resolution of 4-5% is needed to reach the expected  $A'$  mass resolution. The precise reconstruction of the production vertex to reject prompt QED background requires impact parameter resolutions between  $100\text{-}250 \mu\text{m}$  for tracks between  $0.5\text{-}1.7 \text{ GeV}/c$ . These key performance parameters were studied in the HPS Test Run by selecting  $e^+e^-$  pairs from photon conversions. Pairs of oppositely charged tracks, one in the top and one in the bottom half of the SVT, with momentum larger than  $400 \text{ MeV}/c$  were selected and basic distributions of pair production kinematics were studied. The kinematics are relatively well reproduced as shown in Figure 15.

The expected momentum resolution from simulation is between 4-5% for tracks in the momentum range of the HPS Test Run. By comparing, between data and simulation, the shapes of the kinematic distributions for single- and two-track events, we estimate an agreement with the nominal scale and resolution to within 10%.

In the HPS Test Run, as well as in electron running with HPS, the dominant source of uncertainty in the tracking and vertexing is multiple Coulomb scattering. For the vertexing performance the foremost difference compared to electron beam running is that the target was located approximately 67 cm upstream from our nominal target position; giving almost collinear tracks in the detector. The increased lever arm over which tracks are extrapolated widens the resolution with up to a factor of eight (depending on momentum) compared to what is achieved at the nominal electron target position for HPS. Figure 16 shows the horizontal and vertical positions of the extrapolated track at the converter position. While residual alignments show small shifts, the good agreement between data and simulated events of the widths indicates a good understanding of the material budget and distribution in the SVT. Having the

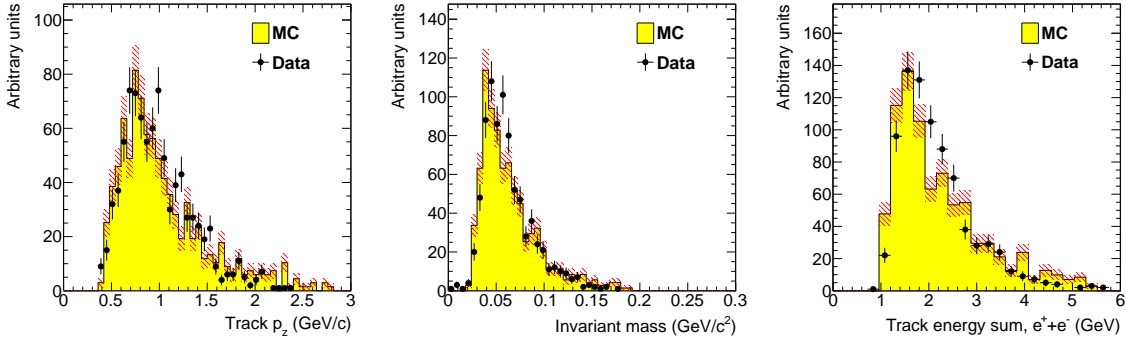


Figure 15: Kinematic distributions for  $e^+e^-$  pairs selected by opposite charged tracks in the top and bottom half of the tracker: track momentum in the top half of the SVT (left), invariant mass (middle) and the sum of the track energy for the pair (right).

779 dominant contribution to the vertex resolution approxi-  
780 mately right demonstrates that the Gaussian part of the  
781 vertex resolution in HPS, with a target at 10 cm, will be  
782 as calculated.

### 783 7.2. ECal Performance

784 During the HPS Test Run 385 out of 442 modules  
785 (87%) were used in offline reconstruction, 39 modules  
786 were disabled or not read out (no FADC channel avail-  
787 able, no APD bias voltage or masked out due to excess-  
788 sive noise) and 18 were masked offline due to noise.

789 The integrated pulse of each FADC channel was con-  
790 verted to energy by subtracting a pedestal and applying  
791 a conversion factor to convert ADC counts to energy.  
792 The pedestals are measured using special runs where  
793 each trigger records 100 samples of signals from the  
794 APDs with 4 ns between each sample. The pedestals  
795 were extracted from the part of the window before the  
796 actual hit in the calorimeter. Modules with signal above  
797 the threshold are clustered using a simple algorithm  
798 similar to the one deployed for the trigger (see Sec. 6.1).  
799 Due to the high effective crystal readout threshold of  
800 73 MeV the average number of crystals in a cluster was  
801  $\sim 3$  and the simple clustering algorithm worked well for  
802 reconstruction of the detected shower energy. An aver-  
803 age noise level of approximately 15 MeV per crystal  
804 was measured in special pedestal runs.

805 The ratio of the ECal cluster energy  $E$  to the momen-  
806 tum  $p$  of a matched track in the SVT was used to de-  
807 termine the conversion factors from ADC counts to en-  
808 ergy. To compare data and simulation, all inoperable or  
809 noisy channels in the SVT and ECal were disabled in  
810 both data and simulation so that any efficiency or bias  
811 that affect the data should be reflected in the simulation.  
812 Iteratively, conversion coefficients for each crystal were  
813 adjusted until the  $E/p$  ratio in data and simulation were

814 similar. The distribution of the  $E/p$  ratio in data and  
815 simulation are compared in Figure 17. The peak position  
816 of the distribution indicates the sampling fraction  
817 of the ECal, the fraction of the incident particle energy  
818 measured in the cluster. The width and tails of the distri-  
819 bution in data indicates imperfect calibration and noise  
820 of the ECal modules. This level of calibration and the  
821 agreement with simulation was found to be sufficient to  
822 study normalized event rates in the HPS Test Run.

823 Since the A' trigger in HPS is relatively insensi-  
824 tive to the energy resolution this level of performance  
825 would be adequate. However, improvements are needed  
826 to achieve the expected energy resolution in HPS ( $< 4.5\%/\sqrt{E}$ ). The noise and thresholds need to be  
827 closer to 10 MeV the thresholds will be lowered and a  
828 more elaborate calibration technique needs to be em-  
829 ployed. In addition the number of working channels  
830 needs to be improved by equipping the detector new and  
831 complete electronics for each channel.

### 833 7.3. Trigger Performance

834 As described above in Sec. 6, the energy from each  
835 crystal is measured differently in the trigger and what  
836 is readout from the ECal. The trigger performance  
837 was studied by simulating the trigger for each event  
838 and comparing to how the events were actually trig-  
839 gered. To eliminate trigger bias, we use a tag and probe  
840 method: to study the trigger performance in one half  
841 of the ECal, we select events which triggered the other  
842 half and where there was exactly one probe cluster in  
843 the ECal half under study. We then measure trigger ef-  
844 ficiency as the fraction of tagged events that fired the  
845 trigger in the probe half as a function of the probe clus-  
846 ter energy, shown in Figure 18. The trigger turn-on is  
847 slow and reaches an uneven plateau at about 700 MeV

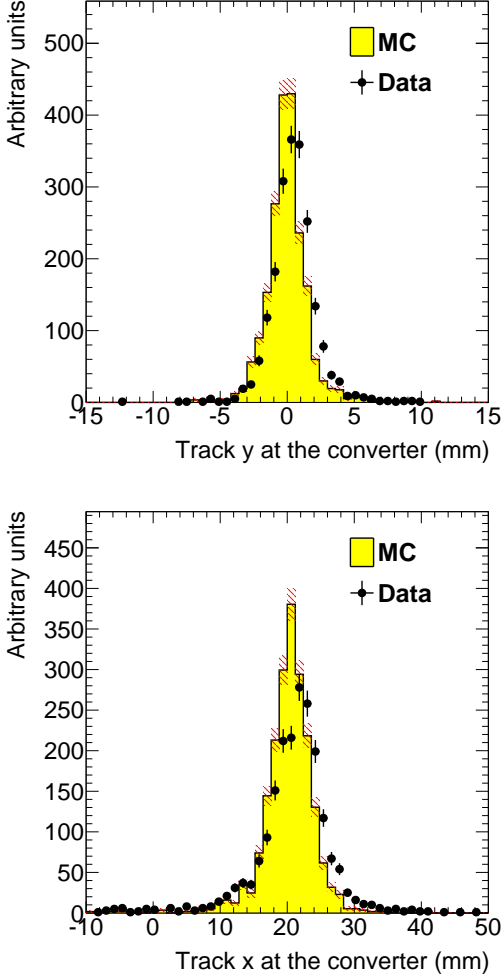


Figure 16: Vertical (top) and horizontal (bottom) extrapolated track position at the converter position taking into account the measured fringe field.

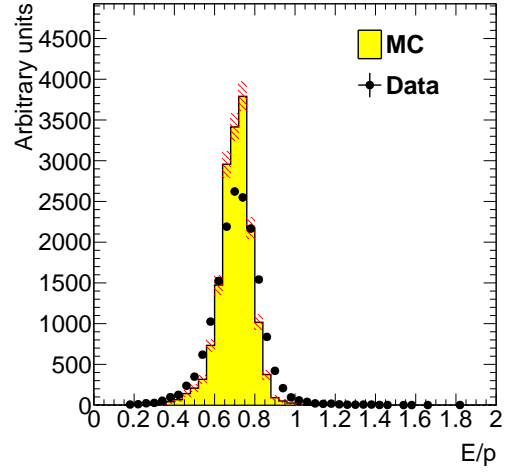


Figure 17: The ECal energy over track momentum ratio ( $E/p$ ) comparing data and simulation for single cluster triggers in the top half of the ECal.

for two reasons; gain variations between different crystals lead to the threshold variations and the nonlinearity of the time-over-threshold integral means that the effective threshold is higher for clusters that span multiple crystals. The effective trigger threshold is therefore dependent on position and energy of the particle as well as cluster multiplicity.

As a cross-check we simulate the FADC trigger path by converting from readout hits (with fixed-size window integration) to trigger hits (time-over-threshold integration). The CTP clustering algorithm and the trigger decision from the SSP are simulated before we compare the trigger decision and trigger time to what was reported by the actual trigger. For every event, the trigger reports the trigger decision as a bit mask (top half, bottom half or both) and the time the trigger fired. The turn-on from the trigger threshold was measured to be 1280 in units of ADC counts as expected. The threshold was not perfectly sharp because of uncertainties in the conversion from readout to trigger hits described above, but based on comparisons with simulation we found that the trigger worked exactly as specified.

#### 7.4. Trigger Rate Comparisons

Trigger rates observed in the HPS Test Run are dominated by multiple Coulomb scattered  $e^+e^-$  pairs in the converter. In simulated events, the rate of triggers depend on the modeling of the pairs' angular distribution and the subsequent multiple Coulomb scattering in the converter. Rates from different converter thicknesses

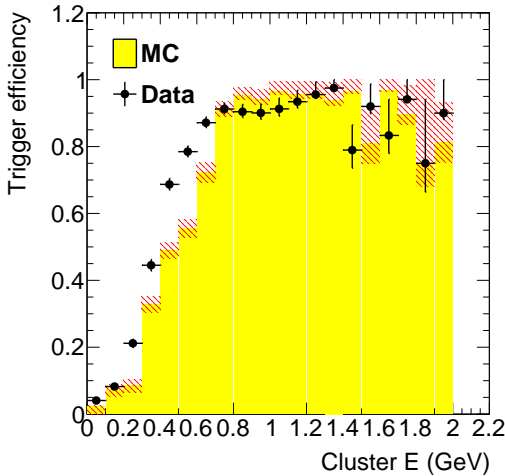


Figure 18: Trigger efficiency in both halves of the ECal for data and simulation as a function of cluster energy.

| Converter (% $X_0$ ) | <b>1.60</b>    | <b>0.45</b>  | <b>0.18</b>  |
|----------------------|----------------|--------------|--------------|
| EGS5                 | $1162 \pm 112$ | $255 \pm 28$ | $94 \pm 17$  |
| Geant4               | $2633 \pm 250$ | $371 \pm 38$ | $114 \pm 18$ |
| Observed             | $1064 \pm 2$   | $196 \pm 1$  | $92 \pm 1$   |

Table 4: Observed and predicted event rate (in Hz) normalized to 90 nA for three different converter thicknesses. The uncertainty on the prediction includes systematic uncertainties from ECal alignment, background normalization, beam current normalization and limited statistics in the simulation.

are used to study the varying multiple Coulomb scattering contribution (pair production angular distribution is constant), and are compared with Geant4 [24] standard multiple scattering model and EGS5 [25]. Restricting clusters to a well calibrated region of the ECal and subtracting the “no converter” background we see agreement with the rates predicted by the EGS5 simulation program, see Table 4. This gives further confidence that the dominant source of background occupancy for HPS, multiple Coulomb scattered beam electrons, is well described.

## 8. Summary and Outlook

The HPS Test Run experiment, using a simplified version of the apparatus planned for the full HPS experiment in a parasitic photon beam, demonstrated the feasibility of the detector technologies proposed for the silicon vertex tracker, electromagnetic calorimeter, and data acquisition systems. Performance from each of these subsystems has been shown to be adequate

to conduct the full experiment successfully with some identified improvements. Studies of multiple Coulomb scattering tails of electrons and positrons from photon conversions further backs expectations from simulation, giving credence to estimates of the detector backgrounds expected in electron beam running for HPS.

## 9. Acknowledgements

The authors are grateful for the support from Hall B at JLab and especially the Hall B engineering group for support during installation and decommissioning. They also would like to commend the CEBAF personnel for good beam performance, especially the last few hours of operating CEBAF6. The tremendous support from home institutions and supporting staff also needs praise from the authors.

This work has been supported by the US Department of Energy, the National Science Foundation, French Centre National de la Recherche Scientifique and Italian Istituto Nazionale di Fisica Nucleare. Rouven Essig is supported in part by the Department of Energy Early Career research program DESC0008061 and by a Sloan Foundation Research Fellowship. Authored by Jefferson Science Associates, LLC under U.S. DOE Contract No. DE-AC05-06OR23177.

## References

- [1] B. Holdom, Two U(1)'s and Epsilon Charge Shifts, Phys.Lett. B166 (1986) 196.
- [2] P. Galison, A. Manohar, TWO Z's OR NOT TWO Z's?, Phys.Lett. B136 (1984) 279.
- [3] R. Essig, J. A. Jaros, W. Wester, P. H. Adrian, S. Andreas, et al. (Report of the Community Summer Study 2013 (Snowmass) Intensity Frontier New, Light, Weakly-Coupled Particles subgroup), Dark Sectors and New, Light, Weakly-Coupled Particles, 2013. URL: <http://arxiv.org/abs/arXiv:1311.0029>.
- [4] M. Pospelov, Secluded U(1) below the weak scale, Phys.Rev. D80 (2009) 095002.
- [5] O. Adriani, et al. (PAMELA Collaboration), An anomalous positron abundance in cosmic rays with energies 1.5-100 GeV, Nature 458 (2009) 607–609.
- [6] M. Ackermann, et al. (Fermi LAT Collaboration), Measurement of separate cosmic-ray electron and positron spectra with the Fermi Large Area Telescope, Phys.Rev.Lett. 108 (2012) 011103.
- [7] M. Aguilar, et al. (AMS Collaboration), First Result from the Alpha Magnetic Spectrometer on the International Space Station: Precision Measurement of the Positron Fraction in Primary Cosmic Rays of 0.5350 GeV, Phys.Rev.Lett. 110 (2013) 141102.
- [8] N. Arkani-Hamed, D. P. Finkbeiner, T. R. Slatyer, N. Weiner, A Theory of Dark Matter, Phys.Rev. D79 (2009) 015014.
- [9] M. Pospelov, A. Ritz, Astrophysical Signatures of Secluded Dark Matter, Phys.Lett. B671 (2009) 391–397.

- 949 [10] J. D. Bjorken, R. Essig, P. Schuster, N. Toro, New Fixed-Target  
 950 Experiments to Search for Dark Gauge Forces, Phys.Rev. D80  
 951 (2009) 075018.
- 952 [11] A. Grillo, et al. (HPS Collaboration), Heavy Photon Search  
 953 Proposal, 2010. URL: [https://confluence.slac.stanford.edu/download/attachments/86676777/HPSProposal-FINAL\\_Rev2.pdf](https://confluence.slac.stanford.edu/download/attachments/86676777/HPSProposal-FINAL_Rev2.pdf).
- 954 [12] A. Sandorfi, et al., 2012. URL: [http://www.jlab.org/exp\\_prog/proposals/06/PR06-101.pdf](http://www.jlab.org/exp_prog/proposals/06/PR06-101.pdf).
- 955 [13] F.-X. Girod, M. Garon (CLAS), Inner calorimeter in clas/dvcs  
 956 experiment, CLAS-Note 2005-001 (2005).
- 957 [14] R. Niyazov, S. Stepanyan (CLAS), Clas/dvcs inner calorimeter  
 958 calibration, CLAS-Note 2005-021 (2005).
- 959 [15] F.-X. Girod (Universite de Strasbourg), 2006. URL: <http://www.jlab.org/Hall-B/general/thesis/fxgirod.pdf>.
- 960 [16] I. Rashevskaya, S. Bettarini, G. Rizzo, L. Bosisio, S. Dittongo,  
 961 et al., Radiation damage of silicon structures with electrons of  
 962 900-MeV, Nucl. Instrum. Meth. A485 (2002) 126–132.
- 963 [17] D. S. Denisov, S. Soldner-Rembold, DO Run IIB Silicon Detec-  
 964 tor Upgrade: Technical Design Report (2001).
- 965 [18] M. French, L. Jones, Q. Morrissey, A. Neviani, R. Turchetta,  
 966 et al., Design and results from the APV25, a deep sub-micron  
 967 CMOS front-end chip for the CMS tracker, Nucl.Instrum.Meth.  
 968 A466 (2001) 359–365.
- 969 [19] M. Friedl, C. Irmler, M. Pernicka, Readout of silicon strip detec-  
 970 tors with position and timing information, Nucl.Instrum.Meth.  
 971 A598 (2009) 82–83.
- 972 [20] H. Dong, et al., Integrated tests of a high speed VXS switch  
 973 card and 250 MSPS flash ADCs, 2007. doi:10.1109/NSSMIC.  
 974 2007.4436457.
- 975 [21] R. Larsen, Emerging New Electronics Standards for Physics,  
 976 Conf.Proc. C110904 (2011) 1981–1985.
- 977 [22] L. Jones, APV25-S1: User guide version 2.2, RAL Microelec-  
 978 tronics Design Group, 2011.
- 979 [23] M. Friedl, C. Irmler, M. Pernicka, Obtaining exact time infor-  
 980 mation of hits in silicon strip sensors read out by the APV25  
 981 front-end chip, Nucl. Instrum. Meth. A572 (2007) 385 – 387.
- 982 [24] S. A. et al., GEANT4 - a simulation toolkit, Nucl.Instrum.Meth.  
 983 A506 (2003) 250 – 303.
- 984 [25] H. Hirayama, Y. Namito, A. Bielajew, S. Wilderman, W. Nelson,  
 985 The EGS5 Code System, 2005.
- 986